ATLAS CONF Note

ATLAS-CONF-2023-058

August 21, 2023

A search for top-squark pair production, in final states containing a t-quark, c-quark and missing transverse momentum, using the full Run 2 dataset collected by the ATLAS detector

The ATLAS Collaboration

This paper presents a search for top-squark pair production in final states with a top quark, charm quark and missing transverse momentum. The dataset was collected with the ATLAS detector during LHC Run 2 and corresponds to an integrated luminosity of 139 fb^{-1} of proton-proton collisions at a centre-of-mass energy of $\sqrt{s}$ = 13 TeV. The analysis is motivated by an extended MSSM model featuring a non-minimal flavour violation in the 2nd and 3rd generation squark sector. The top squark in this model has two possible decay modes, either $\tilde{t}_1 \to c\tilde{\chi}_1^0$ or $\tilde{t}_1 \to t\tilde{\chi}_1^0$. The analysis is optimised assuming both decay modes are equally probable, leading to the most likely final state of $tc + E_{\text{T}}^{\text{miss}}$. Good agreement is found between the post-fit SM expectation and the data in the search regions. Limits are presented in the $\text{m}(\tilde{t}_1)$ vs $\text{m}(\tilde{\chi}_1^0)$ plane and, in addition, limits on the $\text{BR}(\tilde{t}_1 \to t\tilde{\chi}_1^0)$ as a function of $\text{m}(\tilde{t}_1)$ are also produced. Top-squark masses of up to 800 GeV are excluded for scenarios with light neutralinos, and top-squark masses up to 600 GeV are excluded in scenarios where the neutralino and top squark are almost mass degenerate.

ATLAS-CONF-2023-058
13 September 2023

© 2023 CERN for the benefit of the ATLAS Collaboration.
Reproduction of this article or parts of it is allowed as specified in the CC-BY-4.0 license.

1 Introduction

The Standard Model (SM) of particle physics is one of the most comprehensively tested theories of nature, yielding predictions which agree to an incredible extent with a wide range of experimental measurements. However, several aspects of nature remain unexplained by this model despite its success. Amongst them, the experimental mass of the Higgs boson and the possible existence of a non-baryonic component of the universe, called dark matter (DM) [1, 2], pose some of the most important open questions in current particle physics.

Supersymmetry (SUSY) [3–8] is one of the most flexible frameworks extending beyond the SM that can provide an answer to the above questions. By introducing a scalar supersymmetric partner for every chiral component of the standard model fermions[1], it can mitigate large radiative corrections to the Higgs boson mass. These naturalness arguments favour light states for the supersymmetric partners of the top quark, the $\tilde{t}_{\mathrm{L}}$ and $\tilde{t}_{\mathrm{R}}$. The two top squark states mix to yield mass eigenstates $\tilde{t}_1$ and $\tilde{t}_2$, by convention the former being the lightest. Moreover, in R-parity-conserving supersymmetric models [9], supersymmetric partners are produced in pairs, and the lightest supersymmetric particle (LSP) is stable, providing a viable DM candidate. This LSP is generally assumed to be lightest neutralino ($\tilde{\chi}_1^0$).

Searches for the top squark at the LHC experiments have set stringent limits on these particles [10–13], imposing constraints on the $\tilde{t}_1$ mass in the Minimal Supersymmetric Standard Model (MSSM) at the order of 1 TeV, in scenarios where R-parity and flavour are conserved. Extensions of the MSSM can propose scenarios where flavour is not conserved, resulting in looser constraints. In this paper, a non-minimal flavour violation (MFV) extension of the MSSM is considered, as described in [14]. In this framework, the second-generation and third-generation right-handed squark sectors can mix and the mixing is quantified through the mixing angle (θ_{tc}). As consequence of this mixing, the mass eigenstate $\tilde{t}_1$ is a combination of the gauge eigenstates of the 2$^{\mathrm{nd}}$ and 3$^{\mathrm{rd}}$ generation squarks and can decay into a charm quark and a neutralino in addition to decay to the top quark and neutralino, as shown in Figure 1. This search focuses on signals containing on-shell top-quarks produced in the final state, thus signals with $\Delta m(\tilde{t}_1, \tilde{\chi}_1^0) \geq 175$ GeV, and it considers a scan of the branching ratio for $\tilde{t}_1 \rightarrow c\tilde{\chi}_1^0/t\tilde{\chi}_1^0$. Only final states with hadronically decaying tops are considered in the analysis. The advancement of charm-tagging techniques has opened the exploration of charm final states. In particular, those techniques are used in this paper, allowing a first exploration of a signature with both top- and charm-jets at the LHC.

[1] For a generic fermion f, with chiral components f_L and f_R, two scalar fields exist (named respectively $\tilde{f}_L$ and $\tilde{f}_R$).

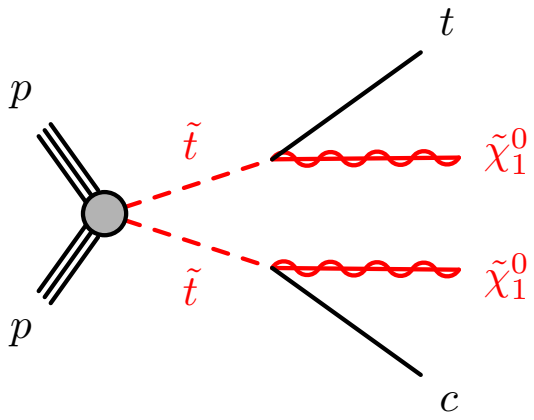

Figure 1: Signal diagram for $\tilde{t}_1$ pair production showing the two possible decay modes of the $\tilde{t}_1$. Decays to pairs of top quarks or charm quarks are also taken into account.

2 ATLAS detector

The ATLAS experiment [15] at the LHC is a multipurpose particle detector with a forward–backward symmetric cylindrical geometry and a near 4π coverage in solid angle.[2] It consists of an inner tracking detector surrounded by a thin superconducting solenoid providing a 2 T axial magnetic field, electromagnetic and hadron calorimeters, and a muon spectrometer. The inner tracking detector covers the pseudorapidity range $|\eta| < 2.5$. It consists of silicon pixel, silicon microstrip, and transition radiation tracking detectors. Lead/liquid-argon (LAr) sampling calorimeters provide electromagnetic (EM) energy measurements with high granularity. A steel/scintillator-tile hadron calorimeter covers the central pseudorapidity range ($|\eta| < 1.7$). The endcap and forward regions are instrumented with LAr calorimeters for both the EM and hadronic energy measurements up to $|\eta| = 4.9$. The muon spectrometer surrounds the calorimeters and is based on three large superconducting air-core toroidal magnets with eight coils each. The field integral of the toroids ranges between 2.0 and 6.0 T m across most of the detector. The muon spectrometer includes a system of precision tracking chambers and fast detectors for triggering. A two-level trigger system is used to select events. The first-level trigger is implemented in hardware and uses a subset of the detector information to accept events at a rate below 100 kHz. This is followed by a software-based trigger that reduces the accepted event rate to 1 kHz on average depending on the data-taking conditions. An extensive software suite [16] is used in data simulation, in the reconstruction and analysis of real and simulated data, in detector operations, and in the trigger and data acquisition systems of the experiment.

3 Data and simulated event samples

The proton-proton collision data analysed in this paper were collected between 2015 and 2018 at a centre-of-mass energy of 13 TeV with a 25 ns proton bunch crossing interval. Multiple pp interactions occur

[2] ATLAS uses a right-handed coordinate system with its origin at the nominal interaction point (IP) in the centre of the detector and the z-axis along the beam pipe. The x-axis points from the IP to the centre of the LHC ring, and the y-axis points upwards. Cylindrical coordinates (r, ϕ) are used in the transverse plane, ϕ being the azimuthal angle around the z-axis. The pseudorapidity is defined in terms of the polar angle θ as $\eta = -\ln\tan(\theta/2)$. Angular distance is measured in units of $\Delta R \equiv \sqrt{(\Delta\eta)^2 + (\Delta\phi)^2}$.

per bunch crossing (pile-up), with an average as measured in data of around 34 interactions. Application of beam, detector and data-quality criteria [17] results in a total integrated luminosity of 139 fb^{-1}. The uncertainty in the combined 2015–2018 integrated luminosity is 1.7% [18], obtained using the LUCID-2 detector [19] for the primary luminosity measurements and cross-checked by a suite of other systems.

Events are required to pass a missing transverse momentum, $E_{\mathrm{T}}^{\mathrm{miss}}$, trigger [20, 21] which is fully efficient for events passing the selections used in the analysis, which requires the offline reconstructed $E_{\mathrm{T}}^{\mathrm{miss}}$ to exceed 250 GeV [21]. To aid with the estimation of some of the SM background processes, events are also selected using single-lepton triggers with corresponding offline thresholds above 27 GeV used to ensure the lepton triggers are also fully efficient.

Samples of Monte Carlo (MC) simulated events are used to model the SUSY signal and background processes in the analysis. The SUSY signal models were generated with MadGraph5_aMC@NLO 2.8.1 [22] at leading order (LO) in QCD and interfaced with Pythia 8.230 [23] for the parton showering (PS) and hadronisation, and with EvtGen 1.6.0 [24] for the modelling of heavy flavour hadron decays. The samples were normalised using the cross-section calculations at next-to-next-to-leading order (NNLO) in the strong coupling constant, adding the resummation of soft gluon emission at next-to-next-to-leading-logarithmic (NNLL) accuracy [25–27]. The signal samples are generated with both possible decays $\tilde{t}_1 \rightarrow t\tilde{\chi}_1^0$ and $\tilde{t}_1 \rightarrow c\tilde{\chi}_1^0$ open and set with a branching ratio (BR) of 50%. This allows a BR scan to be performed by performing a reweighting based upon the number of generated signal events of each decay-type.

SM background samples were generated with different MC event generators depending on the process. Information about the generators and parton showering used for the different processes is shown in Table 1.

For all samples the response of the detector to particles was modelled with the full ATLAS detector simulation [28] based on Geant4 [29]. All simulated events were overlaid with multiple pp collisions simulated with Pythia 8.186 using the A3 tune [30] and the NNPDF2.3LO PDF set. The MC samples were generated with variable levels of pile-up in three campaigns which were reweighted to match the actual distribution of the mean number of interactions observed in data in 2015–2018.

Table 1: Overview of the simulated background samples.

Process	ME event generator and order	ME PDF	PS and hadronisation	UE tune	Cross-section calculation
V+jets ($V = W/Z$)	Sherpa 2.2.1 [31], NLO	NNPDF3.0NNLO	Sherpa	Default	NNLO [32]
Multi-boson	Sherpa 2.2.1-2.2.2[33], NLO	NNPDF3.0NNLO	Sherpa	Default	NLO
$t\bar{t}$	Powheg Box [34], NLO	NNPDF3.0NNLO	Pythia8	A14	NNLO+NNLL [35, 36]
Single top	Powheg Box, NLO	NNPDF3.0NNLO	Pythia8	A14	NNLO+NNLL [37–39]
$t\bar{t}+V$	aMC@NLO 2.3.3, NLO	NNPDF3.0NLO	Pythia8	A14	NLO [22]
tWZ, tZ	aMC@NLO 2.3.3, NLO	NNPDF3.0NLO	Pythia8	A14	NLO

4 Event reconstruction

The analysis uses standard ATLAS reconstruction techniques with the object selections used to define small-R jets, large-R jets, leptons (e, μ), top- and b–tagged jets reported in Table 2. A loose set of requirements on the properties of the candidate objects, are used to define "baseline" objects. The baseline

requirements for each physics object are shown in the second column of Table 2. The physics objects used to define selections and calculate kinematic variables are required to pass tighter selections, referred to as the "signal" requirements, and are presented in the third column of Table 2 . Baseline objects are used to estimate the missing transverse momentum vector ($\vec{p}_{\mathrm{T}}^{\,\mathrm{miss}}$) and its magnitude $E_{\mathrm{T}}^{\mathrm{miss}}$ [40], calculated as the negative vector sum of the transverse momenta of all baseline reconstructed objects and the 'soft term'. The soft term includes all tracks associated with the primary vertex but not matched to any reconstructed lepton or jet. Tracks not associated with the primary vertex are not considered in the $E_{\mathrm{T}}^{\mathrm{miss}}$ calculation, improving its resolution by reducing the effect of pile-up. A quality criterion for the matching of topological cell clusters [41] in the electromagnetic calorimeter to electrons is also imposed in events containing electrons with $|\eta| \in [1.37, 1.52]$ in data recorded during 2015 and 2016.

After the baseline objects are defined, an overlap removal procedure is applied to prevent any double-counting of tracks and energy depositions associated with overlapping jets, electrons and muons. The procedure applies the following actions to the event. First, baseline electrons are discarded if they share a track in the inner detector with a baseline muon. Next, any jet within a distance $\Delta R = \sqrt{(\Delta y)^2 + (\Delta\phi)^2} = 0.2$ of a baseline electron is discarded and the electron is retained, if the jet is *not* identified as a b-tagged jet, otherwise the jet is kept. Similarly, any jet satisfying $N_{\mathrm{trk}} < 3$ (where N_{trk} refers to the number of tracks with $p_{\mathrm{T}} > 500$ MeV that are associated with the jet) within $\Delta R < 0.2$ of a baseline muon is discarded and the muon is retained. Finally, baseline electrons or muons lying within a distance $\Delta R < 0.4$ of a remaining jet are discarded. All "signal" objects are required to pass the overlap removal stage.

For charm tagging, a non-standard, analysis-specific c-tagging algorithm, denoted DL1r$_c$, was optimised. It is based on the DL1r algorithm used for b-tagging [42], which provides three probabilities of the jet coming from the hadronisation of a b-quark (b-jet), a c-quark (c-jet) or a lighter quark/gluon (l-jet). These three probabilities are combined in a similar manner as the b-tagger, but with tuned parameters optimised to identify jets containing c-hadrons. To avoid ambiguities in identifying a jet as both a c- or b-jet, priority is given to b-tagged jets. Namely the two tagging algorithms, DL1r and DL1r$_c$, are run in sequence with the b-tagging algorithm taking precedence and if a jet is classified as a b-jet, it is no longer considered as an input to the c-tagging algorithm. This technique is referred to as *c-tagging with b-veto* technique and is very helpful to avoid a large rate of b-jets misidentified as c-jets. The chosen working point for the b-tagging algorithm is the 77% working point, which corresponds to a misidentification rate of 20% for c-jets and 0.9% for light flavour jets. The working point selected for the c-tagging algorithm (including the effect of the b-veto) corresponds to a 20% c-jet efficiency, with rejection factors of 29 for b-jets and 57 for light-jets, evaluated on simulated $t\bar{t}$ events. Similarities in the decay chain of hadronically decaying tau-leptons and c-hadrons lead to a significant mis-identification efficiency of τ-leptons as charm jets of the order of 15%. Due to this, dedicated variables are defined at event level to reject events containing hadronic τ's, as described in Section 5. The DNN top tagger [43] is used to identify large-R jets which arise from top-quark decays. The 80% efficiency working point is used and is valid for top-tagged jets with masses in the 40–600 GeV range and p_{T} between 350 and 2500 GeV. Large-R jets outside these validity ranges are not identified as arising from a top quark.

Scale factors are applied to account for differences between data and simulation for the trigger, reconstruction, identification and isolation efficiencies. Dedicated scale factors and uncertainties were derived for the specific charm tagging working point used in the analysis to correct for the difference in the simulation to reproduce the charm-tagged jet efficiency and mis-identification rate as measured in data, with the same data-driven techniques as used for b-tagging [42]. In the p_{T} range between 20 and 250 GeV, the correction factors are found to be mostly compatible with unity, with systematic uncertainties ranging from a few % at low p_{T} to a maximum of 15% at higher p_{T}. For higher p_{T} jets the correction is assumed constant and

an additional systematic uncertainty due to the extrapolation is derived using MC simulation, with the uncertainty increasing up to 30% for 3 TeV charm jets.

Table 2: Overview of the baseline and signal physics object definitions. The impact parameter along the beam direction and the significance of the transverse impact parameter are denoted as $z_0 \sin\theta$ and $|d_0/\sigma_{d_0}|$, respectively. Similarly, p_{T}, η and m are the transverse momentum, pseudorapidity and mass, respectively, for each physics object. WP is the considered working point for each jet tagger, corresponding to the listed selection efficiency.

Physics Object	Baseline requirements	Additional Signal requirements
Electrons	Loose likelihood-based selection [44] $z_0 \sin\theta < 0.5$ mm $\|\eta\| < 2.47$ $p_{\mathrm{T}} > 4.5$ GeV	Tight likelihood-based selection [44] $p_{\mathrm{T}} > 10$ GeV Isolation 'Loose' ($p_{\mathrm{T}} > 200$ GeV 'HighPtCaloOnly') [45] $\|d_0/\sigma_{d_0}\| < 5$
Muons	Medium identification [46, 47] $\|\eta\| < 2.7$ $p_{\mathrm{T}} > 4$ GeV	$p_{\mathrm{T}} > 10$ GeV Isolation 'Loose_VarRad' [47] $\|d_0/\sigma_{d_0}\| < 3$
Small-R jets	Particle-flow anti-kt R=0.4 [41, 48–50] $p_{\mathrm{T}} > 20$ GeV $\|\eta\| < 2.8$	Jet vertex tagger > 0.5 and $\|\eta\| < 2.4$ [51] or $p_{\mathrm{T}} > 60$ GeV
Large-R jets	LCTopo trimmed R=1.0 [52] $p_{\mathrm{T}} \geq 200$ GeV $\|\eta\| < 2.0$	
$E_{\mathrm{T}}^{\mathrm{miss}}$		Tight WP [53]
Top-tagged jets		DNN top tagger [43] 80% efficiency WP $p_{\mathrm{T}} \in [350, 2500]$ GeV $m \in [40, 600]$ GeV
b-tagged jets		DL1r tagger [42] 77% efficiency WP
c-tagged jets		DL1r$_c$ tagger 20% efficiency WP

5 Analysis strategy

The kinematics of the SUSY signal under consideration is heavily dependent upon the mass splitting between the top-squark and the neutralino ($\Delta m(\tilde{t}_1, \tilde{\chi}_1^0)$). Generally the phase space can be split into three main regions: the "bulk" region, with large $\Delta m(\tilde{t}_1, \tilde{\chi}_1^0)$; the "intermediate" region where the top-squark and neutralino are relatively close in mass; and finally the "compressed" region, where the mass splitting is such that the top-quark from the $\tilde{t}_1$ decay is produced just on-shell ($\Delta m(\tilde{t}_1, \tilde{\chi}_1^0) \approx m_t$).

The general analysis strategy is to define Signal Regions (SRs) which target different regions of the SUSY signal phase-space by placing selections on particle multiplicities and kinematic variables. Control Regions (CRs) are then defined which are enriched in the main backgrounds present in the SRs, however are orthogonal to the SRs. A likelihood fit is performed where normalisation factors for the main backgrounds are calculated in the CRs and extrapolated to estimate the contributions of these backgrounds in the

SRs. Finally, Validation Regions (VRs) are defined, again orthogonal to SRs and CRs, to investigate the modelling of the backgrounds and confirm the normalisation factor can be extrapolated to the SRs.

Many kinematic variables are employed in the definition of the SRs to isolate the kinematics of the SUSY signals and to reject events arising from the SM background. In addition to selections on the number of b-tagged jets ($N_{b-\text{jets}}$), c-tagged jets ($N_{c-\text{jets}}$), large-R jets compatible with arising from a top-quark ($N_{\text{tops}}^{\text{DNN}}$), $E_{\text{T}}^{\text{miss}}$ and selections on the transverse momentum of the jets ($p_{\text{T}(j/b/c)}$), more complex variables are used, and are described below.

- $\Delta\phi(j_{1-4}, E_{\text{T}}^{\text{miss}})_{\text{min}}$, $\Delta\phi(j_{1-3}, E_{\text{T}}^{\text{miss}})_{\text{min}}$:
  The minimum difference in azimuthal angle between the leading 4 (3) jets and the $E_{\text{T}}^{\text{miss}}$. In zero lepton regions this variable removes the contribution from multi-jet processes which arise from jet mismeasurement leading to "fake" $E_{\text{T}}^{\text{miss}}$ in the final state.

- $m_{\text{T}}(c, E_{\text{T}}^{\text{miss}})_{\text{min}}$, $m_{\text{T}}(b, E_{\text{T}}^{\text{miss}})_{\text{min}}$:
  The minimum value of the transverse mass calculated between any of the c-tagged (b-tagged) jets and the missing transverse momentum vector. The transverse mass (m_{T}) is defined as:

  $$m_{\text{T}} = \sqrt{2p_{\text{T}}(c/b) \cdot E_{\text{T}}^{\text{miss}}(1 - \cos\Delta\phi(c/b, E_{\text{T}}^{\text{miss}}))}.$$

  These variables are used to reduce the contribution from $t\bar{t}$ which has a kinematic end-point of 200 GeV.

- $m_{\text{T}}(c, E_{\text{T}}^{\text{miss}})_{\text{max}}$, $m_{\text{T}}(b, E_{\text{T}}^{\text{miss}})_{\text{max}}$:
  The maximum value of the transverse mass when calculated between any of the c-tagged (b-tagged) jets and the missing transverse momentum vector. Similarly to the above m_{T}, these variables are used to enhance the signal against the $t\bar{t}$ background, as the $t\bar{t}$ background tends to lower values than the signal.

- $m_{\text{T}}(j, E_{\text{T}}^{\text{miss}})_{\text{close}}$:
  The transverse mass calculated between the jet closest in azimuthal angle to the missing transverse momentum vector and the missing transverse momentum vector itself. This variable is used in conjunction with the $\Delta\phi$ variables to remove the contributions from multi-jet proccesses with “fake” $E_{\text{T}}^{\text{miss}}$.

- $E_{\text{T}}^{\text{miss}}$ Sig:
  The global $E_{\text{T}}^{\text{miss}}$ significance, calculated including the parameterisations of all objects, defined as:

  $$E_{\text{T}}^{\text{miss}}\ \text{Sig} = \sqrt{\frac{|\vec{\text{P}}_{\text{T}}^{\text{miss}}|^2}{\sigma_{\text{L}}^2(1-\rho_{\text{LT}}^2)}}.$$

  Here σ_{L} is the momentum resolution after being rotated into the longitudinal (parallel to the $E_{\text{T}}^{\text{miss}}$) direction, and ρ_{LT} is the correlation factor between the longitudinal and transverse momentum resolutions. This variable is used to discriminate between events where the $E_{\text{T}}^{\text{miss}}$ arises from invisible particles in the final state and events where the $E_{\text{T}}^{\text{miss}}$ arises from poorly measured particles [54].

- $m_{\text{T2}}(j_{R=1.0}^{b}, c)$:
  The stransverse mass variable [55], a generalisation of the transverse mass when two semi-invisibly decaying particles are pair-produced, defined as:

  $$m_{\text{T2}}(\mathbf{p}_{\text{T}}^1, \mathbf{p}_{\text{T}}^2, \mathbf{p}_{\text{T}}^{\text{miss}}) = \min_{\mathbf{q}_{\text{T}}^1+\mathbf{q}_{\text{T}}^2=\mathbf{q}_{\text{T}}^{\text{miss}}} \{\max[m_{\text{T}}(\mathbf{p}_{\text{T}}^1, \mathbf{q}_{\text{T}}^1), m_{\text{T}}(\mathbf{p}_{\text{T}}^2, \mathbf{q}_{\text{T}}^2)]\}.$$

In this case the two visible particles in the decay ($\mathbf{p}_{\mathrm{T}}^{1}$, $\mathbf{p}_{\mathrm{T}}^{2}$) are the large-R jet in the event containing a b-tagged jet and the c-tagged jet. If, in a given event, there is more than one large-R jet containing a b-tagged jet, or more than one c-tagged jet, the large-R jet and c-jet with the highest p_{T} are used in the calculation. For the high-mass $\tilde{t}$ signal this variable is expected to extend to large values, whereas for the $t\bar{t}$ background this variable should dramatically drop-off at the top-mass.

- m_{eff}:
  The effective mass, is the scalar sum of the transverse momenta of all jets in the event and the $E_{\mathrm{T}}^{\mathrm{miss}}$, defined as:

  $$m_{\mathrm{eff}} = \sum_{i=0}^{N_{\mathrm{jets}}} p_{\mathrm{T}}(j_i) + E_{\mathrm{T}}^{\mathrm{miss}}.$$

  Generally for the signal scenarios considered, the m_{eff} extends to high values, compared to the SM backgrounds which generally possess lower values of m_{eff}.

Four orthogonal sets of SRs were developed to target the different areas of phase space, with SRA targeting the bulk region, SRB and SRC targeting the intermediate region, and SRD targeting the compressed region. Due to general similarities between the kinematics of the bulk and intermediate regions, SRA, SRB and SRC have generally similar selections and primarily differ based upon the usage of the $m_{\mathrm{T2}}(j^{b}_{R=1.0}, c)$ variable and the number of top-tagged jets present in the event. Due to the similarity between the SRA, SRB and SRC regions, common CRs are used to predict the main SM backgrounds and common VRs are used to validate the background modelling. The kinematics of the SRD region is significantly different, with a selection requiring the presence of initial-state radiation (ISR) applied to boost the sparticle system, providing enough $E_{\mathrm{T}}^{\mathrm{miss}}$ to pass the trigger selection. All SRs require that events contain zero leptons, at least one b-tagged jet, at least one c-tagged jet and high $E_{\mathrm{T}}^{\mathrm{miss}}$.

The full selections used to define the A-, B-, and C-type regions are seen in Table 3. Commonalities between these regions include specific selections based on large values of $E_{\mathrm{T}}^{\mathrm{miss}}$, $E_{\mathrm{T}}^{\mathrm{miss}}$ significance, and the transverse mass ($m_{\mathrm{T}}(c, E_{\mathrm{T}}^{\mathrm{miss}})_{\mathrm{min}}$) between the c-tagged jet and the $E_{\mathrm{T}}^{\mathrm{miss}}$. SRA is kept orthogonal to the SRB region using the number of top-tagged large-R jets ($N_{\mathrm{tops}}^{\mathrm{DNN}}(R = 1.0)$) with SRA requiring at least 1 top-tagged jet whereas SRB requires exactly 0 top-tagged jets. The SRA and SRC regions are orthogonal due to the selection on $m_{\mathrm{T2}}(j^{b}_{R=1.0}, c)$. The SRB and SRC regions are again orthogonal due to the selection on $N_{\mathrm{tops}}^{\mathrm{DNN}}(R = 1.0)$, with SRB requiring zero top-tagged jets whereas SRC requires at least one. This orthogonality allows for a statistical combination of the three SRs when performing the model-dependent fit.

In the phase space targeted by the SRA region, very large values of $m_{\mathrm{T2}}(j^{b}_{R=1.0}, c)$ are expected. To enhance sensitivity to these signals when performing the model dependent interpretation a multi-bin fit is performed and two bins of $m_{\mathrm{T2}}(j^{b}_{R=1.0}, c)$ are used: $[450 - 575]$ and ≥ 575 GeV. For the intermediate region of phase space, lower values of $m_{\mathrm{T2}}(j^{b}_{R=1.0}, c)$ are expected, so instead sensitivity can be enhanced by performing a multi-bin fit in the $m_{\mathrm{T}}(j, E_{\mathrm{T}}^{\mathrm{miss}})_{\mathrm{close}}$ variable. The SRB region is split into three orthogonal regions in the $m_{\mathrm{T}}(j, E_{\mathrm{T}}^{\mathrm{miss}})_{\mathrm{close}}$ variable: $[100 - 150]$, $[150 - 400]$ and ≥ 450 GeV. SRC uses a similar strategy, however with a finer granularity of $m_{\mathrm{T}}(j, E_{\mathrm{T}}^{\mathrm{miss}})_{\mathrm{close}}$ bins: $[100 - 150]$, $[150 - 300]$, $[300 - 500]$ and ≥ 500 GeV. When performing the model-independent fit, the same lower-bounds are used for the SRA, SRB and SRC regions as in the model-dependent fit, however the upper-bounds on the bins are removed, allowing for more general regions than those used for the model-dependent interpretation.

The largest background contribution in SRA, SRB and SRC comes from Z + jets events followed by single-top and/or W + jets . Common CRs are used to estimate the main backgrounds for both the SRA and SRB regions, with a single VR used to validate the background estimation strategy. Two lepton CRs

are used to extract a normalisation factor for the Z + jets background. In these regions the leptons are subtracted from the true $E_{\mathrm{T}}^{\mathrm{miss}}$, and are used as a proxy for neutrinos mimicking the $Z \to \nu\nu$ decay, this "lepton corrected" $E_{\mathrm{T}}^{\mathrm{miss}}$ is denoted by $E_{\mathrm{T},\ell\ell}^{\mathrm{miss}}$ and in the 2L regions is used when calculating all kinematic variables. The CRZAC region is used to normalise the Z + jets process in both the SRA and SRC regions (as both regions require one top-tagged large-R jet). The CRZB region is used to estimate the Z + jets background in the SRB region, where the presence of a top-tagged large-R jet is explicitly vetoed. A single-lepton CRstAC region is used to estimate the single-top contribution in the SRA and SRC regions, by specifically requiring the presence of one top-tagged large-R jet in the event. Due to the subdominant contribution of other potential SM backgrounds, no further CRs are defined and instead the contributions from these processes are taken directly from simulation. A single, 0L VR (denoted VRZABC) is used to validate the modelling of the Z + jets background in all three SRs. This 0L selection is inclusive with respect to the number of top-tagged jets in the event, and hence can be used to validate the modelling across all SRA, SRB, and SRC regions.

Table 3: Analysis selections for the A-, B-, and C-type regions associated with the SRs targeting the bulk and intermediate signal mass scenarios respectively. Selections denoted with an * are split into multiple bins (for the SR considered) when the model-dependent fit is performed and the selection shown in the table is the lower-bound on the selection used for the given region. 'SFOS' indicates that the selected leptons are required to have the same flavour and opposite-sign electric charges, such that they are compatible with the decay of a Z-boson. More information is provided about the fit strategy in the text.

Variable	**SRA**	**SRB**	**SRC**	**VRZABC**	**CRstAC**	**CRZB**	**CRZAC**
Trigger	$E_{\mathrm{T}}^{\mathrm{miss}}$ Trigger					1L Trigger	
Baseline & signal leptons	= 0				= 1 ($p_{\mathrm{T}} \geq 30$ GeV)	= 2 SFOS ($p_{\mathrm{T}} \geq 30$ GeV)	
$E_{\mathrm{T}}^{\mathrm{miss}}$ (GeV)	≥ 250	≥ 300	≥ 250	≥ 250	≥ 250	≤ 150	
$E_{\mathrm{T},\ell\ell}^{\mathrm{miss}}$ (GeV)	–					≥ 250	
$N_{b-\mathrm{jets}}$ & $N_{c-\mathrm{jets}}$	≥ 1 (Leading jet is either b-tagged or c-tagged)						
N_{jets}	≥ 3	≥ 5	≥ 3	$[3-8]$	≥ 3	≥ 5	≥ 3
$p_{\mathrm{T}}(j_1)$ (GeV)	≥ 50					≥ 20	
$\Delta\phi(j_{1-4}, E_{\mathrm{T}}^{\mathrm{miss}})_{\mathrm{min}}$	≥ 0.4				–		
$m_{\ell\ell}$ (GeV)	–					$[76-106]$	
$m_{\mathrm{T}}(c, E_{\mathrm{T}}^{\mathrm{miss}})_{\mathrm{min}}$ (GeV)	≥ 200				≥ 300	≥ 150	–
$m_{\mathrm{T}}(c, E_{\mathrm{T},\ell\ell}^{\mathrm{miss}})_{\mathrm{min}}$ (GeV)	–					≥ 150	
$N_{\mathrm{tops}}^{\mathrm{DNN}}$ ($R = 1.0$)	≥ 1	= 0	≥ 1	–	≥ 1	= 0	1
$p_{\mathrm{T}}(b_1)$ (GeV)	≥ 20	≥ 20	≥ 100	≥ 20	≥ 20	≥ 20	
$p_{\mathrm{T}}(c_1)$ (GeV)	≥ 20	≥ 100	≥ 100	≤ 200	≥ 20	≥ 20	
$p_{\mathrm{T}}(j_2)$ (GeV)	≥ 20	≥ 100	≥ 20	≥ 20	≥ 20	≥ 20	
$p_{\mathrm{T}}(j_4)$ (GeV)	≥ 20	≥ 50	≥ 20	≥ 20	≥ 20	≥ 20	
$m_{\mathrm{T}}(c, E_{\mathrm{T}}^{\mathrm{miss}})_{\mathrm{max}}$ (GeV)	–	≥ 400	–	≤ 400	–	≥ 400	–
$m_{\mathrm{T}}(b, E_{\mathrm{T}}^{\mathrm{miss}})_{\mathrm{max}}$ (GeV)	–	$[200-700]$	–	≥ 200	–	≥ 200	–
$m_{\mathrm{T}}(b, E_{\mathrm{T}}^{\mathrm{miss}})_{\mathrm{min}}$ (GeV)	≥ 200				≥ 300	≥ 200	–
$m_{\mathrm{T}}(j, E_{\mathrm{T}}^{\mathrm{miss}})_{\mathrm{close}}$ (GeV)	≥ 100	≥ 100 *		≥ 150	≥ 200	–	
$E_{\mathrm{T}}^{\mathrm{miss}}$ Sig	≥ 18	≥ 10	≥ 17	$[15-17]$	$[12-22]$	≥ 10	≥ 17
$m_{\mathrm{T2}}(j^b_{R=1.0}, c)$ (GeV)	≥ 450 *	≥ 150	$[200-450]$	–	≥ 200	–	

Due to the phase space targeted by the SRD region the kinematics are dramatically different from the other SRs due to the small mass difference between the $\tilde{t}$ and $\tilde{\chi}_1^0$. An ISR-like selection is used to "boost" the sparticle system providing the large $E_{\mathrm{T}}^{\mathrm{miss}}$ to pass the trigger selection. The full selections used to define all D-type regions are seen in Table 4.

Generally the selections for the SRD region follow a standard ISR-like selection with a high-p_{T} leading-jet which is not b- or c-tagged. Due to the similarity of the signal, with the main SM backgrounds of $t\bar{t}$ and V + jets , a dedicated multi-class neural network (NN) was developed and deployed to isolate the signal against these two main backgrounds.

The NN is trained with only signal events which contain the mixed $tc + E_{\mathrm{T}}^{\mathrm{miss}}$ decay, $t\bar{t}$ and V + jets events which pass a looser 0L ISR-like selection (which is a baseline for the SRD definition) and uses a total of 44 low-level variables such as the jet $p_{\mathrm{T}}, \eta, \phi$, jet multiplicities and flavours to produce three output scores according to the likelihood a given event is signal-like, $t\bar{t}$-like or V + jets -like. A dedicated hyperparameter optimisation is performed with a "leaky ReLU" activation function. The key variables found to be useful by the NN are $E_{\mathrm{T}}^{\mathrm{miss}}$, the b-jet multiplicity and the p_{T} of the two leading jets. A soft-max activation function is applied to the final layer of the NN with cross-entropy loss leading to an output which is a set of scores per event for the three categories of signal-like, $t\bar{t}$-like and V + jets -like. The signal score ("NN signal score") is subsequently used to define the SR. The V + jets ("V + jets score") score is implemented in the W + jets CR, to enhance the W + jets contribution. As defining a region enhanced in $t\bar{t}$ is comparatively simple in the phase space targeted, the output corresponding to $t\bar{t}$ is unused.

In the phase space targeted by SRD large values of m_{eff} are expected. When considering the model-dependent interpretation, a 2D binning in both m_{eff} and $m_{\mathrm{T}}(j, E_{\mathrm{T}}^{\mathrm{miss}})_{\mathrm{close}}$ is employed to further enhance sensitivity to the signal. The binning in m_{eff} is as follows: SRD750, $[750-1000]$; SRD1000, $[1000-1250]$; SRD1250, $[1250-1500]$; SRD1500, $[1500-1750]$; SRD1750, $[1750-2000]$; and SRD2000, ≥ 2000 GeV. The four lowest m_{eff} bins are further subdivided using the $m_{\mathrm{T}}(j, E_{\mathrm{T}}^{\mathrm{miss}})_{\mathrm{close}}$ variable: SRD750 is split into four bins $[0, 100]$, $[100, 200]$, $[200-300]$ and ≥ 300 GeV; SRD1000 is split into three bins $[0, 100]$, $[100, 200]$, ≥ 200 GeV; and both SRD1250 and SRD1500 are split into two bins of $[0, 100]$ and ≥ 100 GeV. In a similar manner to the SRA and SRB regions, when performing the model-independent fit, the lower bound of the m_{eff} selections are used, with the upper bounds removed. For the SRD750 and SRD1000 regions the $m_{\mathrm{T}}(j, E_{\mathrm{T}}^{\mathrm{miss}})_{\mathrm{close}}$ selection is increased to ≥ 200 GeV, whereas for the remaining SRD regions, it is removed.

As the main backgrounds in the SRD region are $t\bar{t}$, W + jets , and Z + jets , three dedicated CRs are defined to estimate the backgrounds from these processes. The CRDZ region is a 2L region where (as in the CRZAC and CRZB regions) the leptons and subtracted from the $E_{\mathrm{T}}^{\mathrm{miss}}$ calculation and mimic neutrinos from the Z-boson decay and the lepton-corrected $E_{\mathrm{T},\ell\ell}^{\mathrm{miss}}$ is used in all calculations. To constrain W + jets and $t\bar{t}$, single-lepton CRs are used (CRDW and CRDtt respectively), which are orthogonal due to the $N_{b-\mathrm{jets}}$ selections used. In these 1L regions, the lepton is added to the jet collection to mimic the scenario where an hadronic-τ in the zero-lepton selection is mis-reconstructed as a jet. Additionally, to ensure a region pure in the W + jets process the output V + jets score of the NN classifier is used. A common 0L VR (VRD) is then used to validate the extrapolation of the three main backgrounds, which is orthogonal to the SR due to an inverted selection on the NN signal score ($[0.0-0.5]$).

As mentioned in Section 3, the $t\bar{t}$ background is modelled using Powheg Box [34]. A mismodelling of the top p_{T} distribution has been observed for these simulated samples at NLO [56, 57]. The top p_{T} is highly correlated with the m_{eff} distribution used in the D-regions, thus CRDtt and VRD region are also binned in m_{eff} in order to respectively correct and validate the $t\bar{t}$ background prediction in the m_{eff}-binned SRD. For

CRDtt, three bins in m_{eff} are considered: CRDtt750, [750 – 1000]GeV; CRDtt1000, [1000 – 1250] GeV and CRDtt1250, ≥ 1250 GeV. The lack of statistics at high-m_{eff} prevents applying a finer binning at high-m_{eff}. This is compensated by a finer binning in the VRD region: VRD750, [750 – 1000]; VRD1000, [1000 – 1250]; VRD1250, [1250 – 1500]; VRD1500, [1500 – 1750] and VRD1750 ≥ 1750 GeV. This latter bin also includes a $E_{\text{T}}^{\text{miss}} < 600$ GeV cut to avoid signal contamination.

Table 4: Analysis selections for the D-type regions associated with the SR which targets compressed signal scenarios. Selections denoted with * are split into multiple bins when the fitting procedure is performed and the selection shown in the table is the lower-bound on the selection used for the given region. More information is provided about the fit strategy performed in the text.

Variable	**SRD**	**CRDtt**	**CRDW**	**CRDZ**	**VRD**
Trigger	$E_{\text{T}}^{\text{miss}}$ Trigger			1L Trigger	$E_{\text{T}}^{\text{miss}}$ Trigger
Number of baseline & signal leptons	= 0	= 1 ($p_{\text{T}} \geq 30$ GeV)		= 2 ($p_{\text{T}} \geq 30$ GeV)	= 0
$E_{\text{T}}^{\text{miss}}$ (GeV)	≥ 250			≤ 100	≥ 250
$E_{\text{T},\ell\ell}^{\text{miss}}$ (GeV)	–			≥ 250	–
N_{jets}	≥ 3 (Leading jet not b- or c-tagged)				
$N_{c-\text{jets}}$	≥ 1				
$N_{b-\text{jets}}$	≥ 1	≥ 2	= 1	≥ 1	≥ 1
$m_{\text{T}}(c, E_{\text{T}}^{\text{miss}})_{\text{min}}$ (GeV)	≥ 100		≥ 150	≥ 100	≥ 100
$p_{\text{T}}(j_1)$ (GeV)	≥ 100				
$p_{\text{T}}(j_4)$ (GeV)	≥ 30				
$E_{\text{T}}^{\text{miss}}$ Sig	≥ 6				
$\Delta\phi(j_{1-3}, E_{\text{T}}^{\text{miss}})_{\text{min}}$	≥ 0.3			–	≥ 0.3
$\Delta\phi(j_{1-3}, E_{\text{T},\ell\ell}^{\text{miss}})_{\text{min}}$	–			≥ 0.3	–
m_{T} (GeV)	–	≥ 30	[30 – 120]	–	–
NN V + jets score	–		≥ 0	–	–
$\Delta\text{R}(b_1, l_1)$	–		≥ 1.8	–	–
$m_{\ell\ell}$ (GeV)	–			[76 – 106]	–
NN signal score	≥ 0.75	≥ 0.0			[0 – 0.5]
m_{eff} (GeV)	≥ 750*	≥ 750 *	–		≥ 750 *

6 Systematic Uncertainties

The effects of many sources of systematic uncertainty on both the signal and background yields are included when performing the likelihood fit through the introduction of nuisance parameters that impact the expectation values of the poissonian terms for each CR and SR bin. The nuisance parameters are described by Gaussian probability density functions, with the standard deviations of the functions corresponding to a specific experimental or theoretical modelling uncertainty. The preferred value of each nuisance parameter is determined as part of the likelihood fit. The fits performed do not significantly alter or constrain the nuisance parameter values relative to the fit input.

The jet energy scale and resolution uncertainties (for both small-R and large-R jets) are derived as a function of the jet p_{T}, η, and flavour, using a combination of data and simulated events, as detailed in Refs. [58, 59]. These uncertainties also take into account the different pile-up conditions during the four years of data-taking.

Uncertainties in the correction factors for the b- and c-tagging identification response are applied to the simulated event samples. The corrections are extracted from dedicated flavour-enriched samples in data [60]. An additional term is included to extrapolate the measured uncertainties to the high-p_{T} region of interest. This term is calculated from simulated events by considering variations on the quantities affecting the b-tagging performance such as the impact parameter resolution, percentage of poorly measured tracks, description of the detector material, and track multiplicity per jet. The dominant effect on the uncertainty when extrapolating to high-p_{T} is related to the different tagging efficiency when smearing the track impact parameters based on the resolution measured in data and simulation.

Uncertainties connected with the lepton reconstruction and identification are included in the fit, and they are found to have a negligible impact. All uncertainties in the final-state object reconstruction are propagated to the reconstruction of the $E_{\mathrm{T}}^{\mathrm{miss}}$, including an additional term taking into account uncertainties in the scale and resolution of the soft term.

The uncertainties related to modelling the SM background processes using MC simulation are taken into account. The modelling uncertainties are assumed to be correlated between different SRs but are uncorrelated between the different processes considered. Uncertainties related to the modelling of the $t\bar{t}$ and single-top processes arise due to the choice of hard-scattering generator and the matching scheme and these uncertainties are evaluated by comparing the nominal samples with an alternative generator (MadGraph5_aMC@NLO). The uncertainty due to the choice of PS and hadronisation model is calculated by comparing the nominal sample with a sample produced with Powheg interfaced to Herwig 7 [61, 62]. Variations of the renormalisation and factorisation scales, the initial- and final-state radiation parameters and PDF sets are also considered [63]. Specifically for the single-top process, a systematic uncertainty corresponding to the interference term between single-top and $t\bar{t}$ (at NLO) is applied by comparing the nominal sample, generated with the diagram removal (DR) scheme, with a dedicated sample generated with the diagram subtraction (DS) scheme. The modelling uncertainties related to the Z + jets and W + jets processes are evaluated using the 7-point renormalisation and factorisation scale variations [64], varying these scales by factors of 0.5 and 2. The matrix element matching and the resummation scales are also varied by 0.5 and 2. A conservative 100% uncertainty is applied to Z + jets events containing both a true b- and c-quark in the final state. For the rare backgrounds which are not normalised in any region (multi-boson, $t\bar{t}V$ and $t + X$) the measured ATLAS cross-section uncertainty on the process is applied. For the SUSY signal scenarios systematic uncertainties are also calculated by varying the factorisation and renormalisation scales, the ISR parameters, and the choice of PDF. The maximum uncertainty for any signal mass scenario is found to be 20%.

The breakdown of the systematic uncertainties in the post-fit background prediction is shown in Figure 2. The contributions are split by model-dependent SR. The total uncertainty shown is not simply the sum in quadrature of the individual uncertainties due to correlations between the components. In the A-type regions, the dominant uncertainty arises from the experimental uncertainties of the large-R jets, driven by the relatively high-p_{T} large-R jets in this region of phase space. In the B-type and C-type regions the main contribution is from the small-R jet uncertainties due to the tight selections on the leading b- and leading c-jet p_{T}. In the D-type regions the main uncertainty is the uncertainty on the background normalisation parameters, as, in comparison to the other SRs, the CRDs and SRD are much kinematically closer and generally the uncertainties are mostly cancelled between the CR and SR, leaving the uncertainty from the background normalisation in the CRs as the dominant systematic uncertainty.

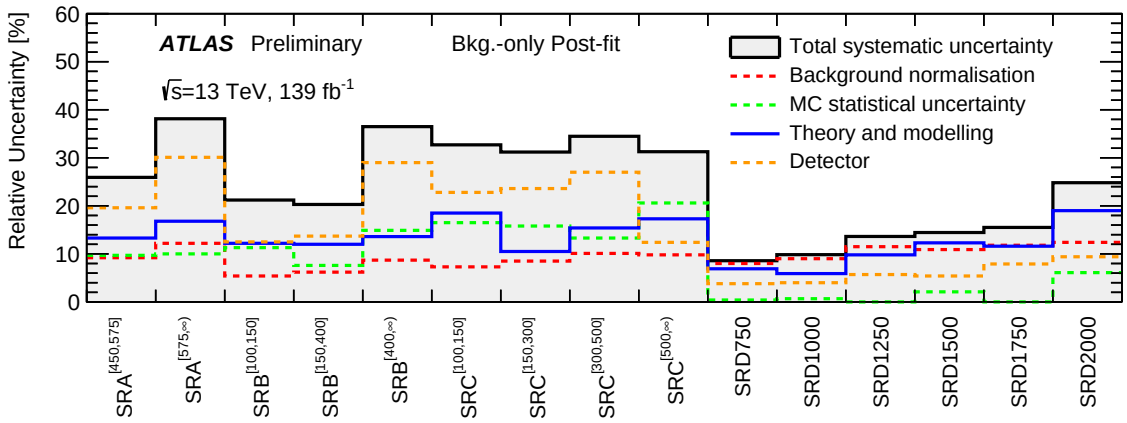

Figure 2: Overview of the systematic uncertainties in the background in the SRs. The 'Detector' category contains all detector-related systematic uncertainties. The 'Background normalization' represents the uncertainty in the fitted normalization factors, including the available data event counts in the CRs. The 'Theory and modelling' represents the theoretical uncertainties of the modelling of the SM background processes. The individual uncertainties may not sum (in quadrature) to the total uncertainty, due to correlations between the different components.

7 Results

Three likelihood fits are performed: the "background-only" fit, which assesses the accuracy of the SM background determination using only the CRs in the fit and extrapolating the normalisation parameters, used to estimate the SM backgrounds, to the SRs; the "model-dependent" fit, which uses both the CRs and SRs to evaluate the confidence-levels (CLs) for a specific BSM hypothesis; and the "model-independent" fit, which is used to calculate the p-value of the SM-only hypothesis [65] again using both the CRs and the SRs.

When performing the background-only fit, the CRs are used in the likelihood and the fitted background estimate is then compared with the observed yields in the VRs and SRs. A single fit is performed using the associated CRs for the A, B, C and D regions, resulting in 7 normalisation parameters. The SM processes which do not have an associated CR are taken to be the values from the MC prediction, however are allowed to float within their own uncertainties in the fit. Concerning the A, B and C regions there are two normalisations, for the Z + jets and single-top backgrounds. For the D regions there are 5 normalisations, one each for W + jets and Z + jets , and 3 normalisations (split over the different m_{eff} bins corresponding to the SRs) for the $t\bar{t}$ background. Due to the different phase-space targeted by the SRD region, the normalisation-factors calculated from the ABC regions are applied solely to the ABC regions, and similarly for the D regions. Figure 3 presents the background-only fit results in the CRs. The normalisations are mostly consistent with unity, aside from the single-top normalisation. A relatively large uncertainty is also found for the single-top normalisation, driven by the comparison between the DR and DS calculation schemes. As the single-top background is sub-dominant and is a relatively small contribution to the SRs, in comparison to the Z + jets background, the single-top normalisation and associated uncertainty is not of great concern.

Generally good agreement is observed between data and post-fit background in all VRs, which is shown

in Figure 4, with a maximum deviation between the observed data and the post-fit SM of less than 2σ, confirming the good modelling of the main background provided by the fit strategy. Finally, Figures 5 and 6 present the post-fit SM yields and observed data in the SRs. For the SRA, SRB and SRC regions the results shown correspond to the selections used for the model-dependent fit, whilst for the SRD regions the region shown is split into the model-dependent m_{eff} and $m_{\text{T}}(j, E_{\text{T}}^{\text{miss}})_{\text{close}}$ bins. The largest background contribution in the SRA and SRB regions is Z + jets followed by single-top. There are deviations from the SM prediction in the fit to the SRs, with a largest deviation of 2σ, generally corresponding to the SRs which contain the tightest $m_{\text{T2}}(j^b_{R=1.0}, c)$ selections. The dominant background in the SRC regions is $t\bar{t}$, followed by V + jets and then single-top production. The post-fit SM is in very good agreement with the data with a largest deficit of 1.8σ in the SRD1500 high-$m_{\text{T}}(j, E_{\text{T}}^{\text{miss}})_{\text{close}}$ bin.

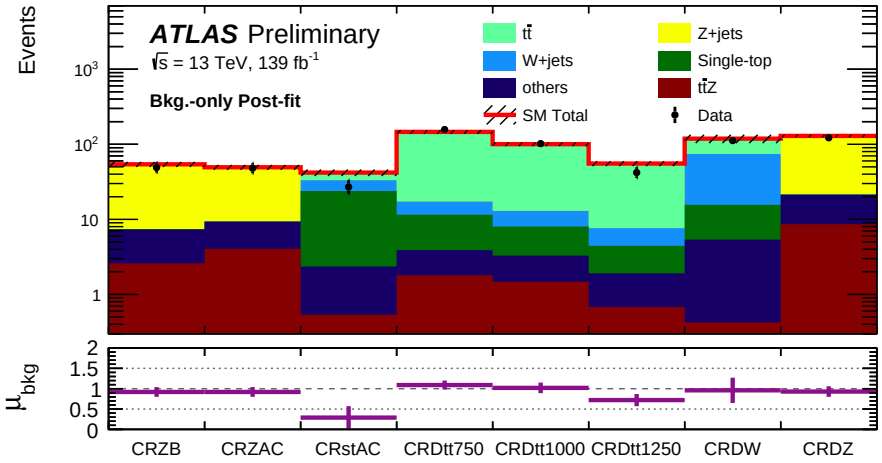

Figure 3: Control region yields and normalisations, derived from the background-only fit. Generally the normalisation parameters are found to be consistent with unity. Both systematic and statistical uncertainties are considered in the error band. The μ_{bkg} label represents the normalisation parameter for the SM background calculated from the relevant CR, for example in CRZB, μ_{bkg} represents the normalisation for the Z + jets background.

Figure 7 presents a selection of key kinematic variables in the SRs, where the arrow shown denotes where the selection on that variable is applied in the relevant region. The $\sim 2\sigma$ discrepancies in the SRA and SRC regions are already present in these distributions. For the SRB and SRD selections it is seen that generally there is nice agreement between the post-fit SM prediction and the observed data.

The model-independent fit is performed by including the signal regions into the likelihood fit as additional constraining bins. As previously discussed, the inclusive SR binning is used to maximise the general sensitivity to new phenomena. A profile-likelihood-ratio statistic is used with a signal of intensity μ_{sig} assumed to contribute only to the SR, and is used to assess the p-value of the background-only hypothesis, and to extract observed and expected 95% confidence level (CL) limits (S^{95}_{obs} and S^{95}_{exp} respectively). The limit on the observed visible cross-section ($\epsilon\sigma^{95}_{\text{obs}}$) is calculated by dividing S^{95}_{obs} by the total integrated luminosity. Table 5 presents these results for the inclusive SRs. The calculated p-values (and thus model-independent limits) generally reflect the 1.8σ differences between the observed and expected yields in the SRs.

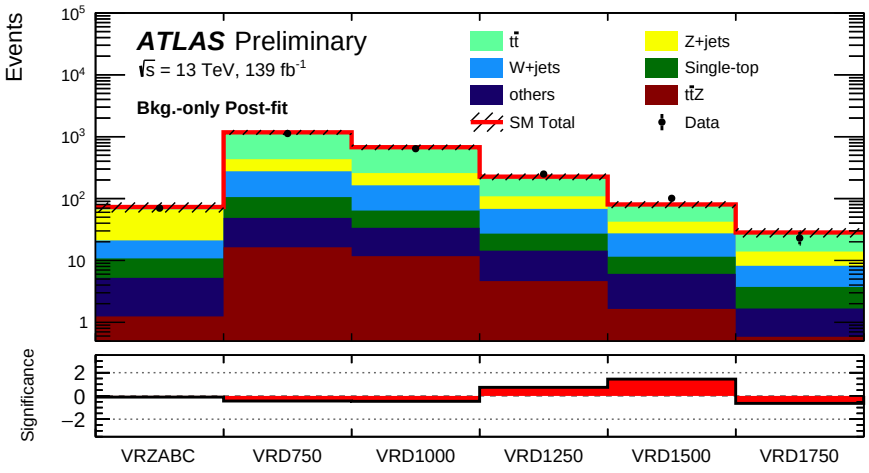

Figure 4: Validation region yields and statistical significance [66], derived from the background-only fit. The post-fit VR yields are found to be consistent within 2σ of the observed data. Both systematic and statistical uncertainties are considered in the error band.

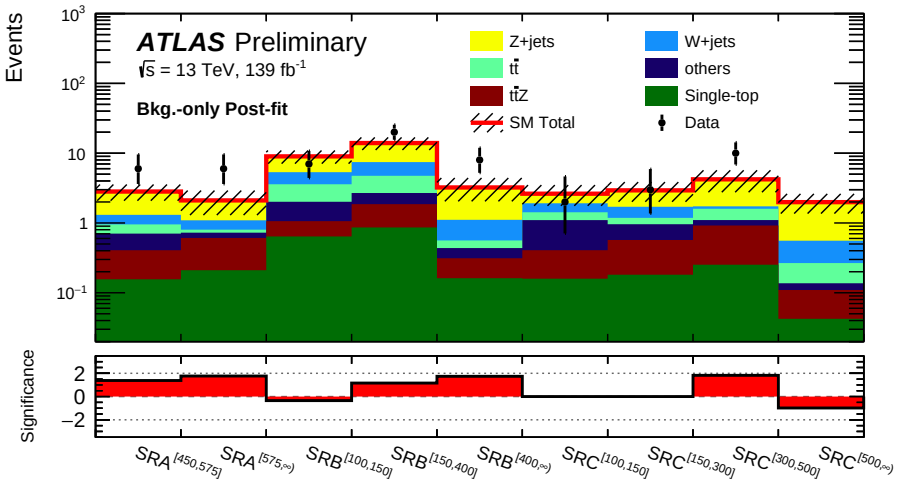

Figure 5: Signal Region yields and statistical significance for the model-dependent fit SRA, SRB and SRC selections. The largest deviation between the post-fit expectation and the observed data is close to 2σ in three regions. Both systematic and statistical uncertainties are considered in the error band.

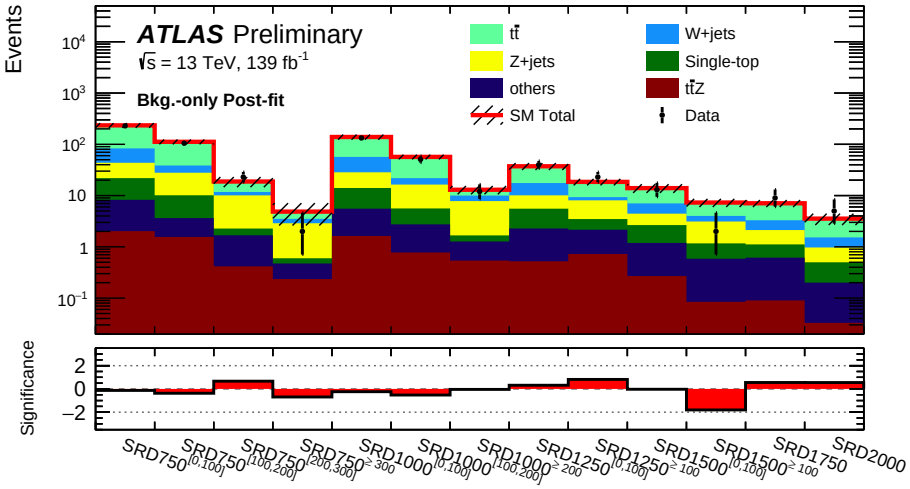

Figure 6: Signal Region yields and statistical significance for the model-dependent fit SRD selections. The largest deviation between the post-fit expectation and the observed data is a 1.8σ deficit in the SRD1500 with $m_{\mathrm{T}}(j, E_{\mathrm{T}}^{\mathrm{miss}})_{\mathrm{close}}$ $\geq$ 100 GeV. Both systematic and statistical uncertainties are considered in the error band.

The model-dependent fit takes into account the contribution of the specific BSM model that is being considered in all CRs and SRs, and considers the full binning in all SRs to greatly enhance the sensitivity to the SUSY signal models considered. The 95% CL exclusion limits on the SUSY signal scenarios are obtained by performing a combined fit of all SRs (increasing the sensitivity using the orthogonal bins as described in Section 5). The result of this combined fit is presented in Figure 8, where the BR($\tilde{t}_1 \rightarrow t + \tilde{\chi}_1^0$)=0.5 is chosen, as this scenario gives the maximal number of $tcE_{\mathrm{T}}^{\mathrm{miss}}$ events. The effect of the 1.8σ over-fluctuation of data in the A and C regions is clearly observed. Despite this, an exclusion up to 800 GeV on top-squark masses is observed for a massless neutralino. In the compressed region, top-squark masses up to 600 GeV are excluded. Figure 9 presents an alternative interpretation, where the neutralino mass is fixed to 1 GeV and the BR of the $\tilde{t}_1 \rightarrow t + \tilde{\chi}_1^0$ decay is allowed to vary between 0 and 1. As expected the maximal sensitivity in this interpretation is where the BR($\tilde{t}_1 \rightarrow t + \tilde{\chi}_1^0$)=0.5. A relatively high sensitivity is still found as the BR moves to 1 for the $\tilde{t}_1 \rightarrow t + \tilde{\chi}_1^0$ decay, primarily arising from the identification of c-jets from W-boson decays. In this scenario, for BR($\tilde{t}_1 \rightarrow t + \tilde{\chi}_1^0$) $\geq$ 0.5, top-squark masses are excluded up to 800 GeV, whereas in the case where BR($\tilde{t}_1 \rightarrow t + \tilde{\chi}_1^0$) = 0 sensitivity is reduced to 600 GeV.

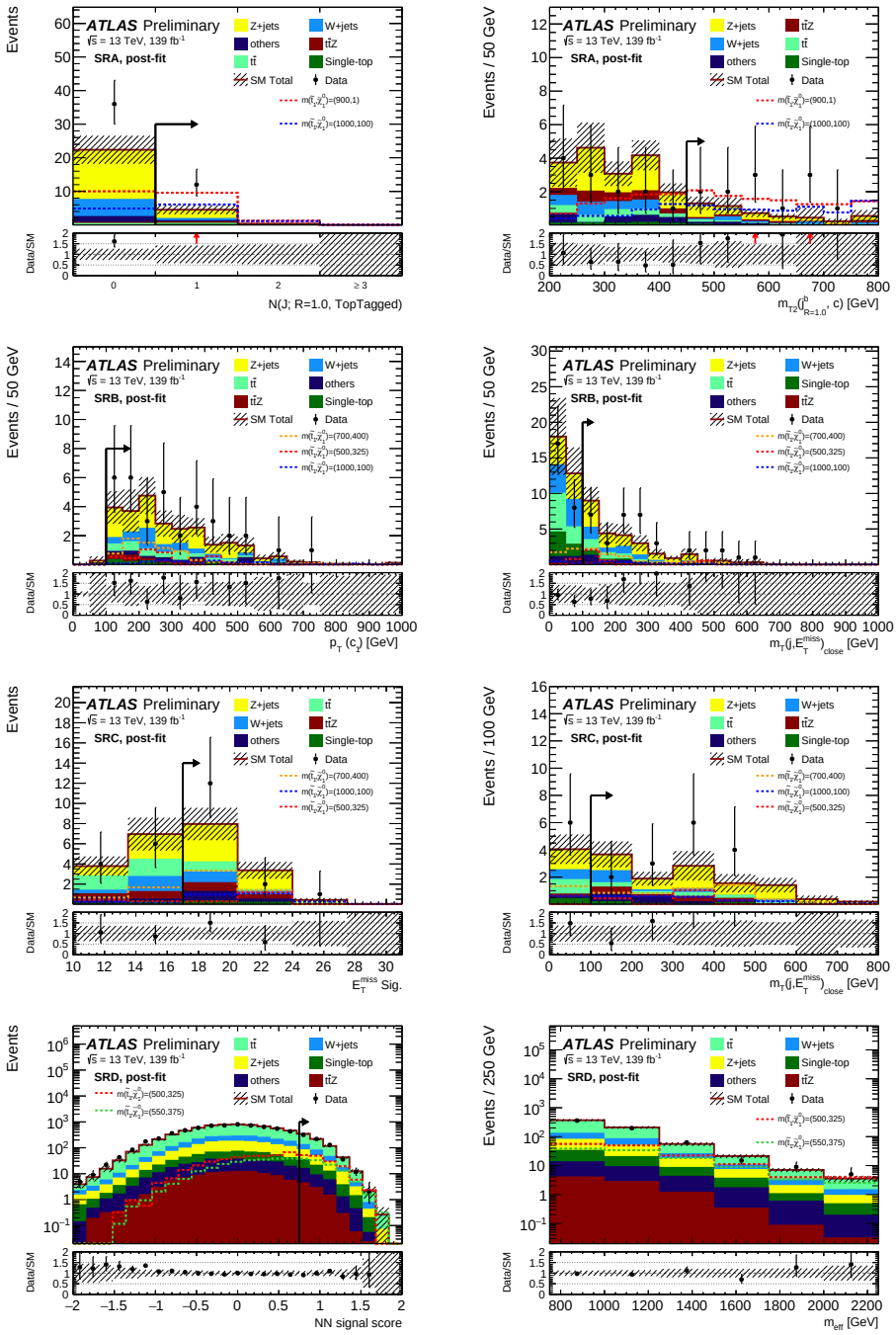

Figure 7: A selection of kinematic distributions in the SRs, presented without the associated SR selection applied to the variable under consideration (except for the SRD m_{eff} distribution at the bottom right plot). The selection applied on the given variable is represented by the arrow. Top row: SRA (left) $N_{\text{tops}}^{\text{DNN}}$; (right) $m_{\text{T2}}(j^{b}_{R=1.0}, c)$. Second row: SRB (left) $p_{\text{T}}(c_1)$; (right) $m_{\text{T}}(j, E_{\text{T}}^{\text{miss}})_{\text{close}}$. Third row: SRC (left) $E_{\text{T}}^{\text{miss}}$ Sig; (right) $m_{\text{T}}(j, E_{\text{T}}^{\text{miss}})_{\text{close}}$. Bottom row: SRD (left) NN signal score; (right) m_{eff}. The right-most bin in each histogram contains the overflow entries. The expected distributions for representative signal scenarios in each analysis region are shown for illustrative purposes.

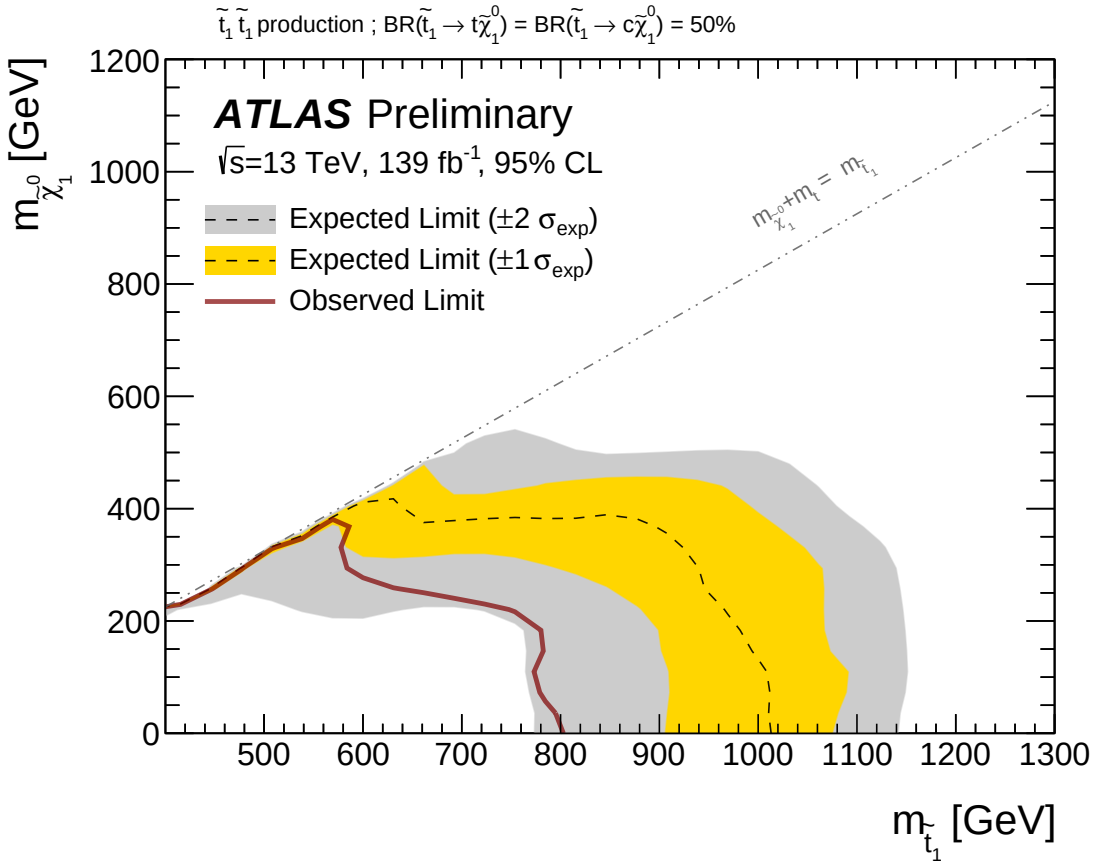

Figure 8: Exclusion limits at the 95% CL in the $\tilde{t}_1$, $\tilde{\chi}_1^0$ mass plane, assuming BR($\tilde{t}_1 \to t + \tilde{\chi}_1^0$) = 0.5. The dashed line, yellow band, and grey band present the expected limit, $\pm 1\sigma$ uncertainty, and $\pm 2\sigma$ uncertainty respectively. The solid red line presents the observed upper limit on the signal cross-section.

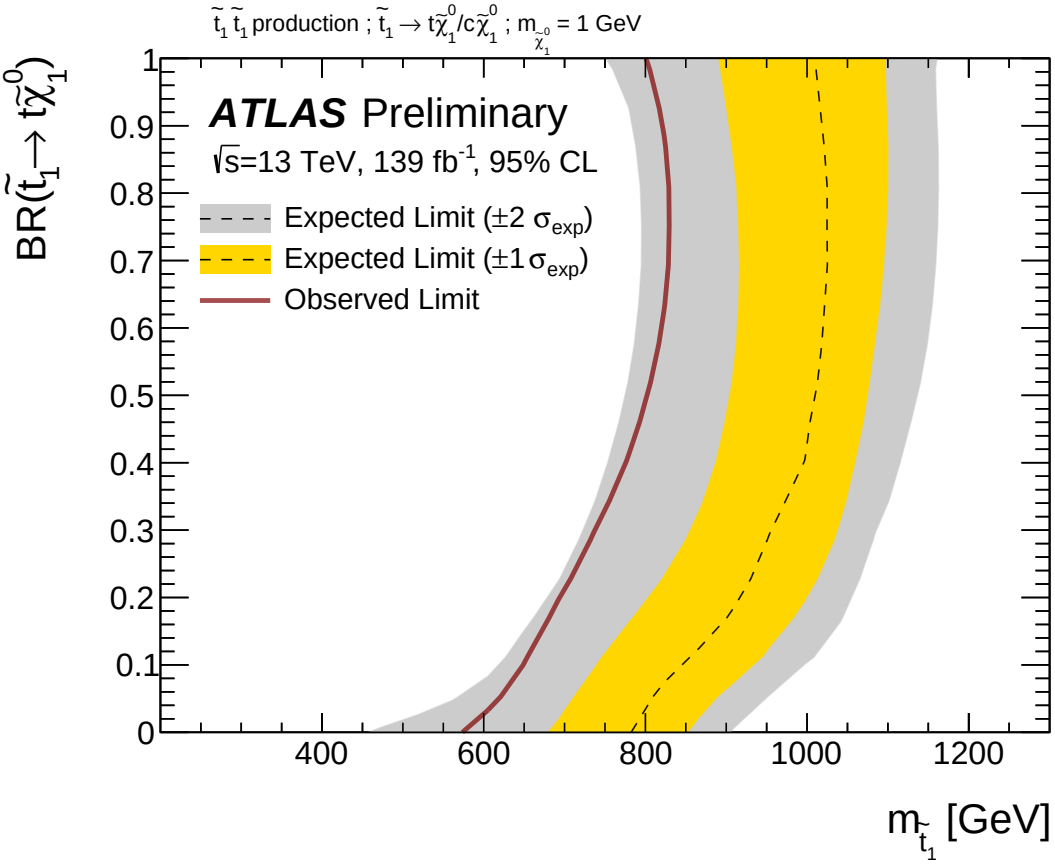

Figure 9: Exclusion limits at the 95% CL in the $\tilde{t}_1$-mass, BR($\tilde{t}_1 \to t + \tilde{\chi}_1^0$) plane, assuming m($\tilde{\chi}_1^0$) = 1 GeV. The dashed line, yellow band, and grey band present the expected limit, $\pm 1\sigma$ uncertainty, and $\pm 2\sigma$ uncertainty respectively. The solid red line presents the observed upper limit on the signal cross-section.

Table 5: Left to right: 95% CL upper limits on the visible cross section ($\langle\epsilon\sigma\rangle^{95}_{obs}$) and on the number of signal events (S^{95}_{obs}). The third column (S^{95}_{exp}) shows the 95% CL upper limit on the number of signal events, given the expected number (and $\pm 1\sigma$ shifts of the expectation) of background events. The last two columns indicate the CL_B value, i.e. the confidence level observed for the background-only hypothesis, and the discovery p-value ($p(s = 0)$).

Signal channel	$\langle\epsilon\sigma\rangle^{95}_{obs}$[fb]	S^{95}_{obs}	S^{95}_{exp}	CL_B	$p(s = 0)$ (Z)
SRA ($m_{\mathrm{T2}}(j^b_{R=1.0}, c) \geq 450$ GeV)	0.10	14	$8.4^{+3.5}_{-1.9}$	0.94	0.02 (2.1)
SRA ($m_{\mathrm{T2}}(j^b_{R=1.0}, c) \geq 575$ GeV)	0.07	9	$5.8^{+2.9}_{-1.2}$	0.89	0.04 (1.7)
SRB ($m_{\mathrm{T}}(j, E^{\mathrm{miss}}_{\mathrm{T}})_{\mathrm{close}} \geq 100$ GeV)	0.17	24	$16.8^{+7.0}_{-5.2}$	0.85	0.09 (1.3)
SRB ($m_{\mathrm{T}}(j, E^{\mathrm{miss}}_{\mathrm{T}})_{\mathrm{close}} \geq 150$ GeV)	0.16	23	$13.2^{+5.5}_{-3.6}$	0.95	0.03 (1.9)
SRB ($m_{\mathrm{T}}(j, E^{\mathrm{miss}}_{\mathrm{T}})_{\mathrm{close}} \geq 400$ GeV)	0.08	11	$6.5^{+3.1}_{-1.6}$	0.92	0.04 (1.8)
SRC ($m_{\mathrm{T}}(j, E^{\mathrm{miss}}_{\mathrm{T}})_{\mathrm{close}} \geq 100$ GeV)	0.09	13	$9.6^{+4.2}_{-2.1}$	0.76	0.22 (0.76)
SRC ($m_{\mathrm{T}}(j, E^{\mathrm{miss}}_{\mathrm{T}})_{\mathrm{close}} \geq 150$ GeV)	0.09	12	$8.7^{+3.9}_{-1.9}$	0.81	0.15 (1.0)
SRC ($m_{\mathrm{T}}(j, E^{\mathrm{miss}}_{\mathrm{T}})_{\mathrm{close}} \geq 300$ GeV)	0.08	11	$7.8^{+3.6}_{-1.7}$	0.83	0.13 (1.1)
SRC ($m_{\mathrm{T}}(j, E^{\mathrm{miss}}_{\mathrm{T}})_{\mathrm{close}} \geq 500$ GeV)	0.02	3	$4.0^{+2.4}_{-1.4}$	0.13	0.50 (0.00)
SRD ($m_{\mathrm{eff}} \geq 750$ GeV,$m_{\mathrm{T}}(j, E^{\mathrm{miss}}_{\mathrm{T}})_{\mathrm{close}} \geq 200$ GeV)	0.15	20	$18.5^{+8.4}_{-5.1}$	0.58	0.50 (0.00)
SRD ($m_{\mathrm{eff}} \geq 1000$ GeV,$m_{\mathrm{T}}(j, E^{\mathrm{miss}}_{\mathrm{T}})_{\mathrm{close}} \geq 200$ GeV)	0.10	14	$13.7^{+3.5}_{-5.7}$	0.52	0.50 (0.00)
SRD ($m_{\mathrm{eff}} \geq 1250$ GeV)	0.30	41	37^{+12}_{-11}	0.60	0.50 (0.00)
SRD ($m_{\mathrm{eff}} \geq 1500$ GeV)	0.09	13	$14.6^{+6.3}_{-4.1}$	0.36	0.50 (0.00)
SRD ($m_{\mathrm{eff}} \geq 1750$ GeV)	0.09	12	$9.1^{+3.9}_{-1.9}$	0.77	0.20 (0.84)
SRD ($m_{\mathrm{eff}} \geq 2000$ GeV)	0.05	7	$5.6^{+3.0}_{-1.2}$	0.70	0.26 (0.64)

8 Conclusion

This paper presented a first search for SUSY signatures leading to a mixed final state containing a top-quark, charm-quark and missing transverse momentum. These results exploit recent top- and charm-tagging techniques.

No significant deviations are observed from the expected background prediction. The largest deviation reaches a significance of 1.8σ in the SRs targeting the bulk and intermediate region of phase space. In the optimal scenario for this analysis, where the branching ratios for the $\tilde{t}_1 \rightarrow t + \tilde{\chi}_1^0$ and $\tilde{t}_1 \rightarrow c + \tilde{\chi}_1^0$ are equal, an exclusion on the top-squark masses up to 800 GeV is found for light neutralinos. In the compressed region, considering the same branching ratio scenario, top-squark masses up to 600 GeV are excluded.

Acknowledgements

We thank CERN for the very successful operation of the LHC, as well as the support staff from our institutions without whom ATLAS could not be operated efficiently.

We acknowledge the support of ANPCyT, Argentina; YerPhI, Armenia; ARC, Australia; BMWFW and FWF, Austria; ANAS, Azerbaijan; CNPq and FAPESP, Brazil; NSERC, NRC and CFI, Canada; CERN; ANID, Chile; CAS, MOST and NSFC, China; Minciencias, Colombia; MEYS CR, Czech Republic; DNRF and DNSRC, Denmark; IN2P3-CNRS and CEA-DRF/IRFU, France; SRNSFG, Georgia; BMBF, HGF and MPG, Germany; GSRI, Greece; RGC and Hong Kong SAR, China; ISF and Benoziyo Center, Israel; INFN, Italy; MEXT and JSPS, Japan; CNRST, Morocco; NWO, Netherlands; RCN, Norway; MEiN, Poland; FCT, Portugal; MNE/IFA, Romania; MESTD, Serbia; MSSR, Slovakia; ARRS and MIZŠ, Slovenia; DSI/NRF, South Africa; MICINN, Spain; SRC and Wallenberg Foundation, Sweden; SERI, SNSF and Cantons of Bern and Geneva, Switzerland; MOST, Taiwan; TENMAK, Türkiye; STFC, United Kingdom; DOE and NSF, United States of America. In addition, individual groups and members have received support from BCKDF, CANARIE, Compute Canada and CRC, Canada; PRIMUS 21/SCI/017 and UNCE SCI/013, Czech Republic; COST, ERC, ERDF, Horizon 2020 and Marie Skłodowska-Curie Actions, European Union; Investissements d'Avenir Labex, Investissements d'Avenir Idex and ANR, France; DFG and AvH Foundation, Germany; Herakleitos, Thales and Aristeia programmes co-financed by EU-ESF and the Greek NSRF, Greece; BSF-NSF and MINERVA, Israel; Norwegian Financial Mechanism 2014-2021, Norway; NCN and NAWA, Poland; La Caixa Banking Foundation, CERCA Programme Generalitat de Catalunya and PROMETEO and GenT Programmes Generalitat Valenciana, Spain; Göran Gustafssons Stiftelse, Sweden; The Royal Society and Leverhulme Trust, United Kingdom.

The crucial computing support from all WLCG partners is acknowledged gratefully, in particular from CERN, the ATLAS Tier-1 facilities at TRIUMF (Canada), NDGF (Denmark, Norway, Sweden), CC-IN2P3 (France), KIT/GridKA (Germany), INFN-CNAF (Italy), NL-T1 (Netherlands), PIC (Spain), ASGC (Taiwan), RAL (UK) and BNL (USA), the Tier-2 facilities worldwide and large non-WLCG resource providers. Major contributors of computing resources are listed in Ref. [67].

References

[1] H. Goldberg, *Constraint on the Photino Mass from Cosmology*, Phys. Rev. Lett. **50** (1983) 1419, Erratum: Phys. Rev. Lett. **103** (2009) 099905.

[2] J. Ellis, J. Hagelin, D. V. Nanopoulos, K. A. Olive, and M. Srednicki, *Supersymmetric relics from the big bang*, Nucl. Phys. B **238** (1984) 453.

[3] Y. Golfand and E. Likhtman, *Extension of the Algebra of Poincare Group Generators and Violation of P Invariance*, JETP Lett. **13** (1971) 323, [Pisma Zh. Eksp. Teor. Fiz. **13** (1971) 452].

[4] D. Volkov and V. Akulov, *Is the neutrino a goldstone particle?*, Phys. Lett. B **46** (1973) 109.

[5] J. Wess and B. Zumino, *Supergauge transformations in four dimensions*, Nucl. Phys. B **70** (1974) 39.

[6] J. Wess and B. Zumino, *Supergauge invariant extension of quantum electrodynamics*, Nucl. Phys. B **78** (1974) 1.

[7] S. Ferrara and B. Zumino, *Supergauge invariant Yang-Mills theories*, Nucl. Phys. B **79** (1974) 413.

[8] A. Salam and J. Strathdee, *Super-symmetry and non-Abelian gauges*, Phys. Lett. B **51** (1974) 353.

[9] G. R. Farrar and P. Fayet, *Phenomenology of the production, decay, and detection of new hadronic states associated with supersymmetry*, Phys. Lett. B **76** (1978) 575.

[10] ATLAS Collaboration, *Search for a scalar partner of the top quark in the all-hadronic $t\bar{t}$ plus missing transverse momentum final state at $\sqrt{s} = 13$ TeV with the ATLAS detector*, Eur. Phys. J. C **80** (2020) 737, arXiv: 2004.14060 [hep-ex].

[11] ATLAS Collaboration, *Search for new phenomena in final states with b-jets and missing transverse momentum in $\sqrt{s} = 13$ TeV pp collisions with the ATLAS detector*, JHEP **05** (2021) 093, arXiv: 2101.12527 [hep-ex].

[12] CMS Collaboration, *Search for top squark production in fully hadronic final states in proton–proton collisions at $\sqrt{s} = 13$ TeV*, Phys. Rev. D **104** (2021) 052001, arXiv: 2103.01290 [hep-ex].

[13] CMS Collaboration, *Search for supersymmetry in proton–proton collisions at 13 TeV in final states with jets and missing transverse momentum*, JHEP **10** (2019) 244, arXiv: 1908.04722 [hep-ex].

[14] A. Chakraborty et al., *Flavour-violating decays of mixed top-charm squarks at the LHC*, Eur. Phys. J. C **78** (2018) 844, arXiv: 1808.07488 [hep-ph].

[15] ATLAS Collaboration, *The ATLAS Experiment at the CERN Large Hadron Collider*, JINST **3** (2008) S08003.

[16] ATLAS Collaboration, *The ATLAS Collaboration Software and Firmware*, ATL-SOFT-PUB-2021-001, 2021, URL: https://cds.cern.ch/record/2767187.

[17] ATLAS Collaboration, *Luminosity determination in pp collisions at $\sqrt{s} = 13$ TeV using the ATLAS detector at the LHC*, (2022), arXiv: 2212.09379 [hep-ex].

[18] ATLAS Collaboration, *Luminosity determination in pp collisions at $\sqrt{s} = 13$ TeV using the ATLAS detector at the LHC*, ATLAS-CONF-2019-021, 2019, URL: https://cds.cern.ch/record/2677054.

[19] G. Avoni et al., *The new LUCID-2 detector for luminosity measurement and monitoring in ATLAS*, JINST **13** (2018) P07017.

[20] ATLAS Collaboration, *Performance of the ATLAS trigger system in 2015*, Eur. Phys. J. C **77** (2017) 317, arXiv: 1611.09661 [hep-ex].

[21] ATLAS Collaboration, *Performance of the missing transverse momentum triggers for the ATLAS detector during Run-2 data taking*, JHEP **08** (2020) 080, arXiv: 2005.09554 [hep-ex].

[22] J. Alwall et al., *The automated computation of tree-level and next-to-leading order differential cross sections, and their matching to parton shower simulations*, JHEP **07** (2014) 079, arXiv: 1405.0301 [hep-ph].

[23] T. Sjöstrand et al., *An introduction to PYTHIA 8.2*, Comput. Phys. Commun. **191** (2015) 159, arXiv: 1410.3012 [hep-ph].

[24] D. J. Lange, *The EvtGen particle decay simulation package*, Nucl. Instrum. Meth. A **462** (2001) 152.

[25] W. Beenakker, M. Krämer, T. Plehn, M. Spira, and P. Zerwas, *Stop production at hadron colliders*, Nucl. Phys. B **515** (1998) 3, arXiv: hep-ph/9710451.

[26] W. Beenakker et al., *Supersymmetric top and bottom squark production at hadron colliders*, JHEP **08** (2010) 098, arXiv: 1006.4771 [hep-ph].

[27] W. Beenakker et al., *Squark and gluino hadroproduction*, Int. J. Mod. Phys. A **26** (2011) 2637, arXiv: 1105.1110 [hep-ph].

[28] ATLAS Collaboration, *The ATLAS Simulation Infrastructure*, Eur. Phys. J. C **70** (2010) 823, arXiv: 1005.4568 [physics.ins-det].

[29] S. Agostinelli et al., *GEANT4 – a simulation toolkit*, Nucl. Instrum. Meth. A **506** (2003) 250.

[30] ATLAS Collaboration, *The Pythia 8 A3 tune description of ATLAS minimum bias and inelastic measurements incorporating the Donnachie–Landshoff diffractive model*, ATL-PHYS-PUB-2016-017, 2016, URL: https://cds.cern.ch/record/2206965.

[31] T. Gleisberg et al., *Event generation with SHERPA 1.1*, JHEP **02** (2009) 007, arXiv: 0811.4622 [hep-ph].

[32] S. Catani et al., *Vector boson production at hadron colliders: A Fully exclusive QCD calculation at NNLO*, Phys. Rev. Lett. **103** (2009) 082001, arXiv: 0903.2120 [hep-ph].

[33] E. Bothmann et al., *Event generation with Sherpa 2.2*, SciPost Phys. **7** (2019) 034, arXiv: 1905.09127 [hep-ph].

[34] S. Alioli, P. Nason, C. Oleari, and E. Re, *A general framework for implementing NLO calculations in shower Monte Carlo programs: the POWHEG BOX*, JHEP **06** (2010) 043, arXiv: 1002.2581 [hep-ph].

[35] M. Cacciari, M. Czakon, M. Mangano, A. Mitov, and P. Nason, *Top-pair production at hadron colliders with next-to-next-to-leading logarithmic soft-gluon resummation*, Phys. Lett. B **710** (2012) 612, arXiv: 1111.5869 [hep-ph].

[36] M. Czakon and A. Mitov, *Top++: A program for the calculation of the top-pair cross-section at hadron colliders*, Comput. Phys. Commun. **185** (2014) 2930, arXiv: 1112.5675 [hep-ph].

[37] N. Kidonakis, *Next-to-next-to-leading-order collinear and soft gluon corrections for t-channel single top quark production*, Phys. Rev. **D 83** (2011) 091503, arXiv: 1103.2792 [hep-ph].

[38] N. Kidonakis, *Two-loop soft anomalous dimensions for single top quark associated production with a W^- or H^-*, Phys. Rev. D **82** (2010) 054018, arXiv: 1005.4451 [hep-ph].

[39] N. Kidonakis, *NNLL resummation for s-channel single top quark production*, Phys. Rev. **D 81** (2010) 054028, arXiv: 1001.5034 [hep-ph].

[40] ATLAS Collaboration, *E_T^{miss} performance in the ATLAS detector using 2015–2016 LHC pp collisions*, ATLAS-CONF-2018-023, 2018, URL: https://cds.cern.ch/record/2625233.

[41] ATLAS Collaboration, *Topological cell clustering in the ATLAS calorimeters and its performance in LHC Run 1*, Eur. Phys. J. C **77** (2017) 490, arXiv: 1603.02934 [hep-ex].

[42] ATLAS Collaboration, *ATLAS flavour-tagging algorithms for the LHC Run 2 pp collision dataset*, (2022), arXiv: 2211.16345 [physics.data-an].

[43] ATLAS Collaboration, *Performance of top-quark and W-boson tagging with ATLAS in Run 2 of the LHC*, Eur. Phys. J. C **79** (2019) 375, arXiv: 1808.07858 [hep-ex].

[44] ATLAS Collaboration, *Electron reconstruction and identification in the ATLAS experiment using the 2015 and 2016 LHC proton–proton collision data at $\sqrt{s} = 13$ TeV*, Eur. Phys. J. C **79** (2019) 639, arXiv: 1902.04655 [hep-ex].

[45] ATLAS Collaboration, *Electron and photon performance measurements with the ATLAS detector using the 2015–2017 LHC proton–proton collision data*, JINST **14** (2019) P12006, arXiv: 1908.00005 [hep-ex].

[46] ATLAS Collaboration, *Muon reconstruction performance of the ATLAS detector in proton–proton collision data at $\sqrt{s} = 13$ TeV*, Eur. Phys. J. C **76** (2016) 292, arXiv: 1603.05598 [hep-ex].

[47] ATLAS Collaboration, *Muon reconstruction and identification efficiency in ATLAS using the full Run 2 pp collision data set at $\sqrt{s} = 13$ TeV*, Eur. Phys. J. C **81** (2021) 578, arXiv: 2012.00578 [hep-ex].

[48] M. Cacciari, G. P. Salam, and G. Soyez, *The anti-k_t jet clustering algorithm*, JHEP **04** (2008) 063, arXiv: 0802.1189 [hep-ph].

[49] M. Cacciari, G. P. Salam, and G. Soyez, *FastJet user manual*, Eur. Phys. J. C **72** (2012) 1896, arXiv: 1111.6097 [hep-ph].

[50] ATLAS Collaboration, *Jet reconstruction and performance using particle flow with the ATLAS Detector*, Eur. Phys. J. C **77** (2017) 466, arXiv: 1703.10485 [hep-ex].

[51] ATLAS Collaboration, *Performance of pile-up mitigation techniques for jets in pp collisions at $\sqrt{s} = 8$ TeV using the ATLAS detector*, Eur. Phys. J. C **76** (2016) 581, arXiv: 1510.03823 [hep-ex].

[52] ATLAS Collaboration, *In situ calibration of large-radius jet energy and mass in 13 TeV proton–proton collisions with the ATLAS detector*, Eur. Phys. J. C **79** (2019) 135, arXiv: 1807.09477 [hep-ex].

[53] ATLAS Collaboration, *Performance of missing transverse momentum reconstruction with the ATLAS detector using proton–proton collisions at* $\sqrt{s} = 13$ *TeV*, Eur. Phys. J. C **78** (2018) 903, arXiv: 1802.08168 [hep-ex].

[54] ATLAS Collaboration,
Object-based missing transverse momentum significance in the ATLAS Detector,
ATLAS-CONF-2018-038, 2018, URL: https://cds.cern.ch/record/2630948.

[55] C. G. Lester and D. J. Summers,
Measuring masses of semi-invisibly decaying particles pair produced at hadron colliders,
Phys. Lett. B **463** (1999) 99, arXiv: hep-ph/9906349.

[56] ATLAS Collaboration, *Measurement of the* $t\bar{t}$ *production cross-section in the lepton+jets channel at* $\sqrt{s} = 13$ *TeV with the ATLAS experiment*, Phys. Lett. B **810** (2020) 135797,
arXiv: 2006.13076 [hep-ex].

[57] ATLAS Collaboration, *Inclusive and differential cross-sections for dilepton* $t\bar{t}$ *production measured in* $\sqrt{s} = 13$ *TeV pp collisions with the ATLAS detector*, (2023), arXiv: 2303.15340 [hep-ex].

[58] ATLAS Collaboration, *Jet energy scale measurements and their systematic uncertainties in proton–proton collisions at* $\sqrt{s} = 13$ *TeV with the ATLAS detector*, Phys. Rev. D **96** (2017) 072002,
arXiv: 1703.09665 [hep-ex].

[59] ATLAS Collaboration, *Jet energy resolution in proton–proton collisions at* $\sqrt{s} = 7$ *TeV recorded in 2010 with the ATLAS detector*, Eur. Phys. J. C **73** (2013) 2306, arXiv: 1210.6210 [hep-ex].

[60] ATLAS Collaboration, *Measurement of b-tagging efficiency of c-jets in* $t\bar{t}$ *events using a likelihood approach with the ATLAS detector*, ATLAS-CONF-2018-001, 2018,
URL: https://cds.cern.ch/record/2306649.

[61] M. Bähr et al., *Herwig++ physics and manual*, Eur. Phys. J. C **58** (2008) 639,
arXiv: 0803.0883 [hep-ph].

[62] J. Bellm et al., *Herwig 7.0/Herwig++ 3.0 release note*, Eur. Phys. J. C **76** (2016) 196,
arXiv: 1512.01178 [hep-ph].

[63] ATLAS Collaboration,
Improvements in $t\bar{t}$ *modelling using NLO+PS Monte Carlo generators for Run 2*,
ATL-PHYS-PUB-2018-009, 2018, URL: https://cds.cern.ch/record/2630327.

[64] E. Bothmann, M. Schönherr, and S. Schumann,
Reweighting QCD matrix-element and parton-shower calculations, Eur. Phys. J. C **76** (2016) 590,
arXiv: 1606.08753 [hep-ph].

[65] M. Baak et al., *HistFitter software framework for statistical data analysis*,
Eur. Phys. J. C **75** (2015) 153, arXiv: 1410.1280 [hep-ex].

[66] R. D. Cousins, J. T. Linnemann, and J. Tucker,
Evaluation of three methods for calculating statistical significance when incorporating a systematic uncertainty into a test of the background-only hypothesis for a Poisson process,
Nucl. Instrum. Meth. A **595** (2008) 480, arXiv: physics/0702156 [physics.data-an].

[67] ATLAS Collaboration, *ATLAS Computing Acknowledgements*, ATL-SOFT-PUB-2021-003, 2021,
URL: https://cds.cern.ch/record/2776662.